Exploring recollision of ultrafast electrons from photoelectron momentum distributions using single-cycle near-infrared laser pulses

Ming-Hu Yuan [1,*] André D. Bandrauk,[2] and Xue-Bin Bian [1]

[1]*State Key Laboratory of Magnetic Resonances and Atomic and Molecular Physics, Wuhan Institute of Physics and Mathematics, Innovation Academy for Precision Measurement Science and Technology, Chinese Academy of Sciences, Wuhan 430071, China*
[2]*Laboratoire de Chimie Théorique, Faculté des Sciences, Université de Sherbrooke, Sherbrooke, Québec J1K 2R1, Canada*

The electron scattering process has been investigated by analyzing the interference structure in the photoelectron momentum distribution (PMD) of a hydrogen atom exposed to a single-cycle linearly polarized near-infrared laser field, based on the numerical solution of the full-dimensional time-dependent Schrödinger equation and the Coulomb correlative classical trajectory simulation. The interference pattern in the PMD is closely related to the form of the ultrashort pulse which is dominated by the carrier-envelope phase. A fish-bone-like pattern appears in the PMD using the sine electric field and a spider-like pattern appears using the cosine electric field. These interference structures reflect the scattering process. It is found that the stripe density of the spider-like pattern is mainly dominated by the recollision time of scattering electron trajectories, i.e., the longer the recollision time, the greater the stripe density. Therefore, the photoelectron interference pattern can be used to understand the ionization and scattering processes, and identify these processes on the attosecond time scale.

I. INTRODUCTION

When ultrafast intense linearly polarized lasers interact with atoms or molecules, electron wave packets will be ionized and accelerated in the oscillatory field, then part of them may be driven back and recollide with the parent ion when the laser electric field changes sign. The returning electron can either recombine with the parent ion, releasing its kinetic energy as a photon, or can be elastically scattered from the potential of the ion [1,2]. This simple scattering mechanism [3–6] governs many strong-field ionization processes such as high-order harmonic generation [7], high-order above-threshold ionization [8], nonsequential double ionization [9], photoelectron holography [10], and so on. The electrons undergoing the scattering process have the potential to probe the dynamic structure of atoms, molecules, or materials on the angstrom length scale and attosecond time scale.

The photoelectron momentum distribution (PMD) of atoms exposed in an intense laser field provides both temporal and structural information about ionizing electrons with unprecedented accuracies [11,12]. In the PMD, various patterns appear because of the interference between different photoelectron wave packets [13], e.g. the photoelectron hologram [14,15] formed by the direct ionization electron wave packet and the scattering electron wave packet. Similarly to optical interferometry, the scattering electron wave packet, which encodes the information of the core, is taken as the signal wave, while the directly ionized wave packet is regarded as the reference wave. Recently, Huismans *et al.* [16,17] and Hickstein *et al.* [18] reported a spider-like pattern

experimentally, which is formed by the interference between the forward scattering electron packet and the direct ionization wave packet. On the other hand, a distinctly different structure was predicted theoretically [19,20], i.e. the fish-bone-like pattern which is formed by the interference between the backscattering electron wave packet and the direct ionization wave packet. Subsequently, the structure was identified experimentally and employed to retrieve information on nuclear dynamics [21]. In a word, these interference patterns in PMDs are caused by two photoelectron wave packets that arrive at a detector with the same final momentum but different phases because of the various quantum paths and flying time [22,23]. The long wavelength was thought initially to be crucial for the observation of holography, but it was also observed with near-infrared (NIR) laser pulses soon after [24,25].

In general, the interference pattern in PMD is influenced by the pulse duration. In a multicycle laser field, electron wave packets are released from their parent ion repeatedly with every optical cycle, then both intracycle and intercycle interferences exist simultaneously and interplay in the whole interaction process [11,12]. Thus, it is hard to extract the electron scattering dynamics information from the PMD. A few-cycle laser pulse is a favorable choice to investigate the scattering process, where only intracycle interference and an unambiguous pattern appear in the PMD [26–28]. The electron scattering process is influenced sensitively and even controlled by the carrier-envelope phase (CEP) of the few-cycle pulse [29]. More recently, Murakami and Zhang [30] reported that interference patterns in a PMD change dramatically with CEPs in the few-cycle regime and that CEP-stable few-cycle laser pulses can be used to identify different types of intracycle interference. However, it is still unclear how the scattering process affects the interference structures in the

*mhyuan@wipm.ac.cn

PMD and which character of the recollision electrons can be reflected from the details of these structures.

In the present work, we solve the full-dimensional time-dependent Schrödinger equation (TDSE) in the length gauge to explore the recollision of ultrafast electrons when a hydrogen atom is illuminated by a single-cycle linearly polarized NIR laser field. In the numerical calculation, we split the wave function into internal and external parts in the time propagation to eliminate the boundary effects, i.e., the reflection of electron wave packets [31]. In addition, a Coulomb correlative classical trajectory (CCCT) method is introduced to analyze the photoelectron scattering process. The PMD is simulated by extracting the classical phase difference between the scattering electron trajectories (STs) and the nonscattering (direct) electron trajectories (DTs).

We find that the interference pattern in the PMD is closely related to the form of the electric field, which is dominated by the CEP obviously for the ultrashort pulse. A fish-bone-like pattern appears in the PMD for an electric field with sine shape, but for a cosine shaped electric field an absolutely different spider-like pattern appears. Then we compare the stripe density of the spider-like pattern with the change of CEP using both the TDSE and CCCT methods and find it is varied sensitively. It is concluded that the stripe density depends on the recollision time of STs. At the end, we also provide the PMDs of hydrogen atoms exposed in the cosine shaped electric field but with different wavelengths. The results reveal that the recollision time of STs is shorter and the stripe density is sparser for the pulse with short wavelength than that with long wavelength. This agrees well with the results in Ref. [30].

This paper is organized as follows. In Sec. II, we briefly mention the theoretical methods, i.e., the full-dimensional TDSE method solved in spherical coordinates, extraction of the PMD, and the CCCT method. In Sec. III, we give the results and discussions. Then we summarize our conclusions in Sec. IV. Atomic units are used throughout, except when otherwise stated.

II. METHODOLOGY

A. Full-dimensional time-dependent Schrödinger equation

The electron distribution of an atomic system has spherical symmetry, which is usually described in spherical coordinates (r, θ, ϕ), e.g., the wave function is expanded by a series of products of radial wave functions and angular wave functions [32]. When the atomic system interacts with a linearly polarized laser pulse, the electron wave function (including the bound and ionized electrons) will be cylindrically symmetric around the direction of laser polarization. Thus, the azimuthal angle ϕ of the spherical coordinates is free for this interaction, and the electron wave function can be expanded as

$$\psi(\mathbf{r}, t) = \sum_{l=0}^{l_{\max}} \sqrt{\frac{2l+1}{4\pi}} \frac{\chi_l(r, t)}{r} P_l(\theta). \quad (1)$$

Here, the reduced radial wave function $\chi_l(r, t)$ is represented on the basis of sine-DVR (sine basis functions are used to define the discrete variable representation) [33,34], and $P_l(\theta)$ is the Legendre polynomial. l is the angular quantum number. Based on this representation, we can benefit from angular

momentum theory when dealing with the angular degrees of freedom.

The TDSE has been solved with the single-active-electron and dipole approximations in the length gauge,

$$i \frac{\partial}{\partial t} \psi(\mathbf{r}, t) = \left(-\frac{\nabla^2}{2} + V^{(a)}(r) + V^{(F)}(\mathbf{r}, t) \right) \psi(\mathbf{r}, t), \quad (2)$$

where $V^{(a)}(r)$ represents the atomic potential and $V^{(F)}(\mathbf{r}, t) = \mathbf{r} \cdot \mathbf{E}(t)$ is the laser-atom interaction. We define the polarization vector of the linearly polarized laser field along the z axis,

$$\mathbf{A}(t) = \frac{E_0}{\omega} f(t) \cos(\omega t + \varphi) \hat{\mathbf{z}}, \quad (3)$$

with φ being the CEP, ω being the laser frequency, $f(t) = \sin^2(\omega t / 2N)$ being the envelope, and N being the number of the optical cycles. Then, the electric field is given by $\mathbf{E}(t) = -\dot{\mathbf{A}}(t)$. The second-order split-operator scheme is employed to propagate the wave function fast and efficiently.

B. Photoelectron momentum distribution

To eliminate the boundary effects, the wave function ψ is split into internal ψ_{in} and external ψ_{ex} parts at a given time t_k in the propagation as [31]

$$\psi(\mathbf{r}, t_k) = f_{\text{abs}}(r, \delta t) \psi(\mathbf{r}, t_k) + [1 - f_{\text{abs}}(r, \delta t)] \psi(\mathbf{r}, t_k)$$
$$= \psi_{\text{in}}(\mathbf{r}, t_k) + \psi_{\text{ex}}(\mathbf{r}, t_k), \quad (4)$$

where

$$f_{\text{abs}}(r, \delta t) = \begin{cases} e^{-\delta t V_0 \left(\frac{r - r_0}{r_{\max} - r_0} \right)^2} & (r_0 < r < r_{\max}), \\ 1 & (0 < r < r_0). \end{cases} \quad (5)$$

Here, $t_k = k \delta t$, and δt is much larger than the integration time dt (we set $\delta t = 200 dt$). V_0 and r_0 are the absorption coefficient and boundary, respectively. ψ_{in} is propagated with dt under the full Hamiltonian numerically. ψ_{ex} stands for the wave function in the outer region ($r_0 < r < r_{\max}$), and it is propagated in momentum space under the Volkov Hamiltonian analytically [35,36].

At each time t_k, a series of operations need to be performed as follows. First, we calculate the external wave function in the velocity gauge using the formula

$$\psi_v^{(k)}(\mathbf{r}, t_k) = \exp[-i[\mathbf{A}(t_k) - \mathbf{A}(t_0)] \cdot \mathbf{r}] \psi_{\text{ex}}(\mathbf{r}, t_k). \quad (6)$$

At the initial moment t_0, the laser intensity is zero, i.e., $A(t_0) = 0$. Next we calculate the wave function in momentum space by Fourier transform,

$$\Psi_v^{(k)}(\mathbf{p}, t_k) = \frac{1}{2\pi} \iint \exp[-i\mathbf{p}\mathbf{r}] \psi_v^{(k)}(\mathbf{r}, t_k) d\mathbf{r}. \quad (7)$$

Then the momentum wave function $\Psi_v^{(k)}(\mathbf{p}, t_k)$ is propagated to the final time t_f,

$$\Psi_v^{(k)}(\mathbf{p}, t_f) = U(t_f, t_k) \Psi_v^{(k)}(\mathbf{p}, t_k), \quad (8)$$

where $U(t_f, t_k)$ is the field propagator,

$$U(t_2, t_1) = \exp \left(-\frac{i}{2} \int_{t_1}^{t_2} [p^2 + 2A(t)p + A(t)^2] dt \right). \quad (9)$$

The final photoelectron momentum wave function can be obtained by adding all of the momentum wave functions at each time t_k,

$$\Psi_v(\mathbf{p}, t_f) = \sum_k \Psi_v^{(k)}(\mathbf{p}, t_f). \tag{10}$$

The PMD is expressed as $D(\mathbf{p}) = |\Psi_v(\mathbf{p}, t_f)|^2$. After the end of the laser pulse, the time evolution is continued for more cycles without any external field to make sure all ionized wave packets enter into the outer region. In other words, the final photoelectron momentum wave function includes all of the ionized wave packets by the long time propagation.

C. Coulomb correlative classical trajectory method

In this subsection, we consider the classical description of an electron in a laser electric field with the nonrelativistic approximation, where the magnetic field is negligible. Then, the electronic dynamics are governed by the Newton-Lorentz equation [37],

$$\frac{d\mathbf{v}}{dt} = -\mathbf{E}_{\text{total}}. \tag{11}$$

In this equation, we keep the influence of Coulomb potential in the time evolution of each electron trajectory. Based on a specific initial trajectory condition, the time-dependent velocity and position of photoelectrons can be easily integrated,

$$\mathbf{v}(t) = -\int_{t_i}^t \mathbf{E}(t')dt' + \int_{t_i}^t \mathbf{F}[\mathbf{r}(t')]dt' + \mathbf{v}_i, \tag{12a}$$

$$\mathbf{r}(t) = \int_{t_i}^t \mathbf{v}(t')dt' + \mathbf{r}_i, \tag{12b}$$

where t_i, $\mathbf{v}_i$, $\mathbf{r}_i$, and $\mathbf{F}$ are the ionization moment, initial velocity, initial position, and Coulomb force which is a function of the position. We solve the equations by numerical iterative method and choose a sufficiently small interval time δt for convergent results.

When the electron is driven by a linearly polarized field, we assume that the initial velocity right after tunneling is perpendicular to the polarization direction of the laser field but the initial position is along this direction, i.e., $v_{\text{per}}^i = |v_i|$, $v_{\text{par}}^i = 0$ and $r_{\text{per}}^i = 0$, $r_{\text{par}}^i = \pm|r_i|$, where $r_i = I_p/E_0$ [I_p is the ionization potential, $r_{\text{par}} < 0$ for $E(t_i) > 0$ and $r_{\text{par}} > 0$ for $E(t_i) < 0$]. Therefore, the classical phase for any trajectory can be obtained by integrating the kinetic energy of the photoelectron,

$$S = \int_{t_i}^{t_f} \frac{v_{\text{per}}(t)^2 + v_{\text{par}}(t)^2}{2}dt + I_p(t_i - t_0), \tag{13}$$

where the first item integrated from the ionization moment to the end of pulse is the action by the external field and Coulomb potential, while the second item implies the phase accumulation of electron before ionization [8].

III. RESULTS AND DISCUSSION

In our wave-function-splitting scheme, $r_0 = 150$ a.u., $r_{\text{max}} = 300$ a.u., and the radial spatial interval is $dr = 0.1$ a.u. The absorption coefficient V_0 equals 3.0. $dt = 0.017$ a.u., so

$\delta t = 200 dt = 0.025$ cycle; i.e., the value of δt is much less to speed up the simulations. In our calculation, all of the free parameters (r_0, r_{max}, v_0, and δt) satisfy the physical conditions which were listed in Ref. [31]. In the angular dimensionality, we chose the angular quantum number l to be no more than 70 for the internal wave function, which converge in our calculations.

In Figs. 1(a) and 1(b), we plot the electric field $E(t)$ and its corresponding vector potential $A(t)$ of single-cycle linearly polarized laser fields with different CEPs. There are two peaks with the same magnitude but in the opposite directions for the sine form of $E(t)$ with $\varphi = 0°$ and a single main peak for the cosine form of $E(t)$ with $\varphi = -90°$. The laser peak intensity and wavelength are the same for the two cases, i.e., $I_0 = 2.0 \times 10^{14}$ W/cm^2 and $\lambda = 1000$ nm. The peak strengths of the laser electric field and vector are $E_0 = 0.075$ a.u. and $A_0 = 1.675$ a.u., respectively. We get the corresponding ADK ionization rate [38] for the two pulses as shown by the gray filled areas. Obviously, there is an ionization peak at the moment of maximum electric field amplitude, as shown by the two and one peaks of the ionization rate for the sine and cosine fields, respectively. Figures 1(c) and 1(d) show the TDSE simulated PMDs of the hydrogen atom exposed in the above fields, whose polarization direction is parallel to the z axis ($\theta = 0°$ and $180°$ in spherical coordinates). The PMD for the electric field with the sine shape ($\varphi = 0°$) features a fish-bone-like pattern; see Fig. 1(c). What is more, the momenta of photoelectrons mainly distribute in the range of $p_z > 0$ (p_z is parallel to the laser polarization direction), and the distribution is symmetrical with respect to the polarization axis. According to the strong-field approximation (SFA), which neglects the Coulomb influence in the ionization process, and supposing a null initial momentum, the final momentum is equal to the negative vector potential when the electron is just ionized, that is, $\mathbf{P} = -\mathbf{A}(t_i)$. Both the backward rescattering holography [19] and time double-slit interference [28,39] demonstrated this fish-bone-like structure. It is hard to disentangle them since the stripe position and density are quite close. Considering the small rescattering section, the double-slit interference should be dominant. On the other hand, when we change the CEP of the single-cycle laser pulse from $\varphi = 0°$ to $\varphi = -90°$, an absolutely different spider-like pattern appears [see Fig. 1(d)], which indicates the interference between the forward scattering electron wave packet and the direct ionization electron packet [19,20]. The PMD is also distributed in the range of $p_z > 0$, which is the same as that in Fig. 1(c). In the cosine electric field, there is only one ionization peak [see the gray filled area in Fig. 1(b)] in the second and third quarter-cycles where the signs of vector potential are opposite. Thus, the spider-like pattern is formed by the photoelectron wave packet ionized in the third quarter-cycle when the vector potential is negative. Hence one can see that the recollision processes are closely dependent on the symmetry of the single-cycle pulse. For the sine electric field, the ionization moments of recolliding and directly ionized electrons are in different quarter-cycles when the directions of vector potential are opposite. This indicates backward rescattering of the recollision. In contrast, forward rescattering appears in the cosine electric field. These features have been obtained in some experiments and theoretical
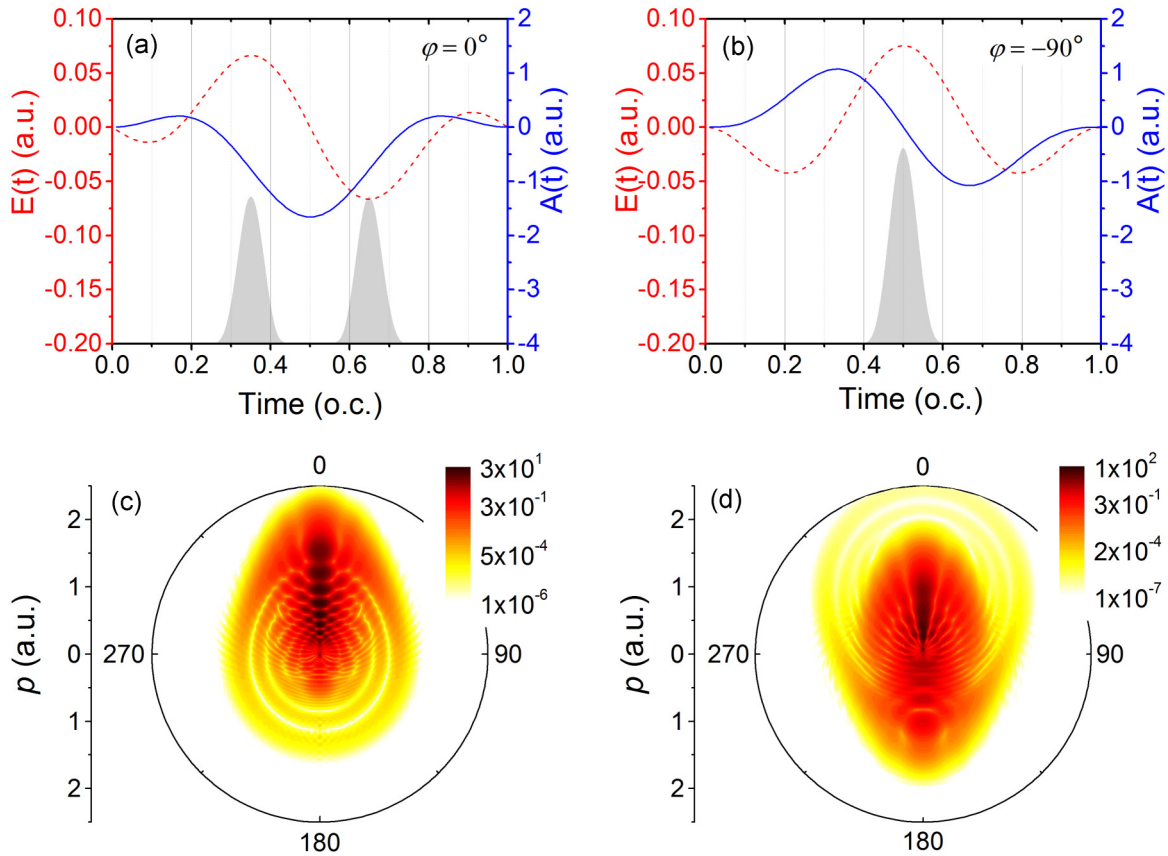
FIG. 1. The single-cycle linearly polarized laser fields with different carrier-envelope phases (CEPs) and the corresponding photoelectron momentum distributions (PMDs) of hydrogen atoms. The electric field $\mathbf{E}(t)$ (red dash curve) and its corresponding vector potential $\mathbf{A}(t)$ (blue solid curve) are shown, with the CEPs of $\varphi = 0°$ (a) and $\varphi = -90°$ (b) ("o.c." denotes optical cycle). The gray filled areas indicate the ADK ionization rate. The same laser peak intensity and wavelength are $I_0 = 2.0 \times 10^{14}$ W/cm^2 and $\lambda = 1000$ nm ($E_0 = 0.075$ a.u. and $A_0 = 1.675$ a.u.), respectively. The PMDs are shown in spherical coordinates, where the positive p_z is along $0°$ and the negative p_z is along the $180°$. The PMD is featured by a fish-bone-like pattern when the electric field has a sine shape ($\varphi = 0°$) (c) and a spider-like pattern for the cosine electric field ($\varphi = -90°$) (d).

models [16–20,27,40]. However, in-depth discussion about some characteristics of the PMD with different CEPs, which reflect the dynamics of scattering electrons, is still lacking; for example, the density of the "spider legs" in the forward scattering interference pattern.

Hickstein *et al.* [18] have demonstrated that the number of the "spider legs" is associated with the times the electron is driven across its parent ion in the laser field. Meanwhile, Huismans *et al.* [17] have reported that the fringe spacing is independent of the laser pulse duration and changes slightly with intensity but significantly with wavelength. Here, we distinguish the most simple single recollision electrons using single-cycle cosine linearly polarized laser pulses to investigate the scattering dynamics of electrons by analyzing the spider-like structures of PMDs. In Figs. 2(b), 2(c), and 2(d), the PMDs of hydrogen exposed in laser fields with a series of different CEPs $\varphi = -60°$, $-70°$, and $-80°$ are displayed, and the corresponding ADK ionization rates are exhibited in Fig. 2(a). As shown, only one ionization peak appears for these cosine-like pulses, and clear spider-like structures emerge in all three PMDs. These features are similar to those in the cosine shape pulses, which implies that there are mainly forward scattering and direct ionization electrons in these

laser fields. Furthermore, the electrons are scattered by their parent ion only once because of the short pulse. In order to observe the density of the "spider legs," we extract the photoelectron momentum angular distributions (PMADs) by integrating the PMDs along the radial coordinate in a small range ($0.45 < p < 0.55$ a.u.) around a particular value which is smaller than the cutoff momentum [18], as shown in Fig. 3. In view of the symmetry of PMDs, the PMADs as functions of polar angle are extracted in the range of $0° < \theta < 90°$. Obviously, the peaks are the most dense for the case of $\varphi = -60°$, then thinned out successively for the cases of $\varphi = -70°$ and $\varphi = -80°$, and the most sparse for the case of $\varphi = -90°$. In addition, the modulation depths between the peaks are different for the four cases, which indicates the various relative strengths of the scattering and direct ionization paths. The closer the ionization intensities of the two paths are, the deeper the modulation depth will be.

We then simulated the interferential structure between STs and DTs using the CCCT method. In this classical simulation, the momentum is equal to the velocity (in atomic units), i.e., $\mathbf{v} = \mathbf{p}$. The electron will be always affected by the Coulomb potential and external field simultaneously after tunneling. If the trajectory is affected by the Coulomb potential weakly,
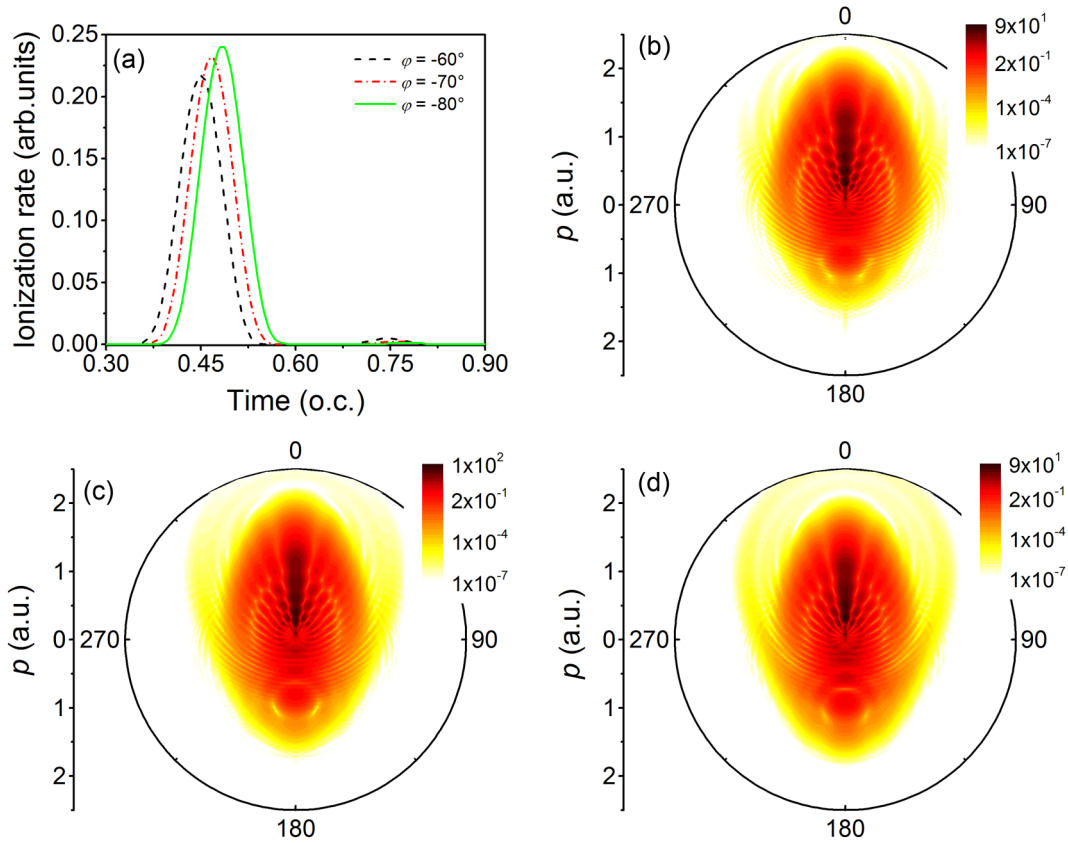
FIG. 2. The ADK ionization rates for single-cycle laser fields with different CEPs (a) and the corresponding PMDs of hydrogen atoms [(b) $\varphi = -60°$, (c) $\varphi = -70°$, (d) $\varphi = -80°$]. A single major ionization peak appears for all three situations which means there are only forward scattering electron orbits, exactly as in the case of the spider-like patterns in (b)–(d). The intensity and wavelength are the same as those used in Fig. 1.

which is not strong enough to change the trajectory direction, then the final perpendicular momentum (p_{per}) has the same sign as that of the initial velocity ($v^i_{per}p_{per} > 0$); we name it DT. Contrarily, if the final perpendicular momentum has
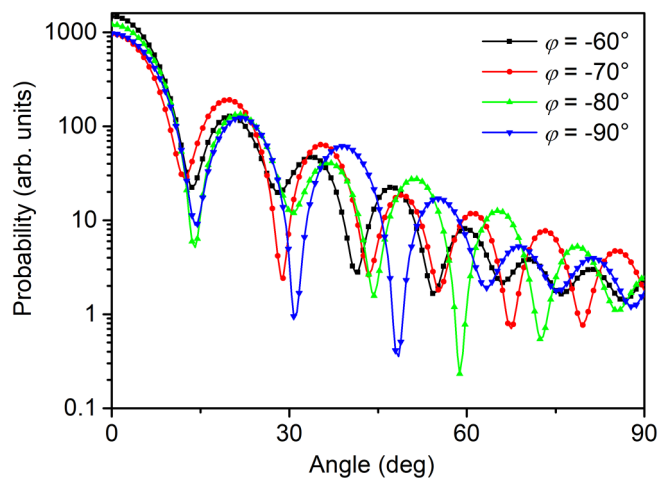

FIG. 3. Photoelectron momentum angular distributions (PMADs) by integrating the PMDs along the radial momentum in the range of $0.45 < p < 0.55$ a.u. The CEPs are $\varphi = -60°$, $-70°$, $-80°$, and $-90°$, respectively. The other laser parameters are the same as those used in Fig. 1. The PMADs as functions of polar angle are extracted in the range of $0° < \theta < 90°$.

a sign opposite to that of the initial velocity ($v^i_{per}p_{per} < 0$) because of the strong effect of the Coulomb potential, we name it ST [41,42]. Figure 4(a) shows the probabilites of ST and DT as a function of the initial condition (i.e., the ionization moment and initial momentum) when a hydrogen atom is exposed in a cosine electric field. We set the initial momentum in the range of [0, 1.0] a.u. and all the trajectories start in the third quarter-cycle, from which the ionized electrons correlate reciprocally and form the forward scattering interferential pattern (spider-like). The probability is calculated by the ADK method for a given initial condition. The same final momentum of the ST and DT is necessary for interference, thus we average all the physical parameters (such as ionization moment, initial momentum, recollision time, phase, and so on) of every electron trajectory within every final momentum bin in the two-dimensional momentum space [27]. It is clear that the two types of trajectories are mainly decided by the initial velocity, i.e., the DTs have a larger initial velocity perpendicular to the polarization direction of the laser field than that of the STs. The electrons with a large initial transversal velocity will deviate from thier parent ion quickly, thus be affected weakly by the Coulomb potential. The phase of every trajectory can be obtained easily using Eq. (13), and the interference map in the momentum plane (p_{par}, p_{per}) is calculated by $[1 + \cos(\Delta S)]/2$ in Fig. 4(b), where ΔS is the phase difference of STs and DTs. The interferential structure is similar to the spider-like pattern in
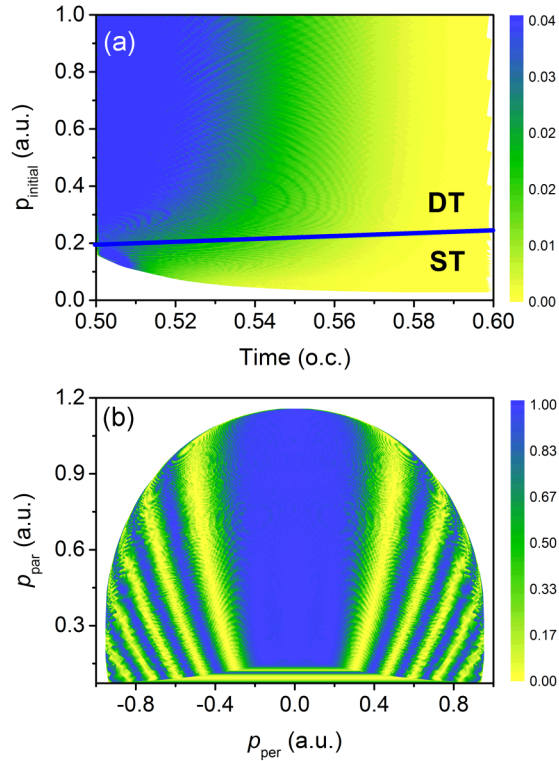
FIG. 4. (a) Probability of STs and DTs as a function of the initial conditions (the ionization moment and initial momentum), calculated by the CCCT method. The two types of trajectories are divided by the thick blue line. A single-cycle linearly polarized laser pulse with CEP of $\varphi = -90°$, wavelength of $\lambda = 1000$ nm, and peak intensity of $I_0 = 2.0 \times 10^{14}$ W/cm^2 is chosen. (b) Interferential structure between the STs and DTs obtained by the CCCT method, which corresponds to the spider-like pattern in PMD as shown in Fig. 1(d).

FIG. 5. (a) The interferential structures between the STs and DTs obtained by CCCT for the laser pulses with CEPs of $\varphi = -60°$, $-70°$, $-80°$, and $-90°$. The other laser parameters are the same as those used in Fig. 4. Here, the range of $0.45 < p_{\text{par}} < 0.55$ a.u. is chosen for clear comparison between the four cases. (b) The average peak widths (PWs) calculated by the TDSE and CCCT methods with different CEPs. The PW$_{\text{TDSE}}$ is extracted in the angular dimension from Fig. 3 and the PW$_{\text{CCCT}}$ is extracted in the perpendicular momentum dimension from (a) when $p_{\text{par}} = 0.5$ a.u..

the PMD, and the vertical stripes can be analogous to the "spider legs."

In order to seek the reason for the change of the stripe density in the forward scattering PMD (the density of "spider legs") as shown in Fig. 3, we calculate the interferential structures between the STs and DTs using the CCCT method for single-cycle linearly polarized laser pulses with CEPs of $\varphi = -60°$, $-70°$, $-80°$, and $-90°$ in Fig. 5(a). Here, we show the interferential patterns in the range of $0.45 < p_{\text{par}} < 0.55$ a.u., which is the same as the integral range used in Fig. 3. The streaks are the most dense for the case of $\varphi = -60°$ (the top row), then thinned out successively for the cases of $\varphi = -70°$ (the second row) and $\varphi = -80°$ (the third row), and the most sparse for the case of $\varphi = -90°$ (the bottom row). This feature agrees well with that of the results from TDSE. Furthermore, the direct quantitative relation between the stripe density and CEP is given by the TDSE and CCCT methods in Fig. 5(b). Thus the CEP of a laser pulse can be obtained directly according to the interference pattern characteristics. Here, we label the stripe density with the average peak widths (PWs), which are extracted in the angular dimension and perpendicular momentum dimension by the TDSE and CCCT methods, respectively.

In Fig. 6(a), we plot the electric fields and their corresponding vector potentials of the four laser pulses. The maximum
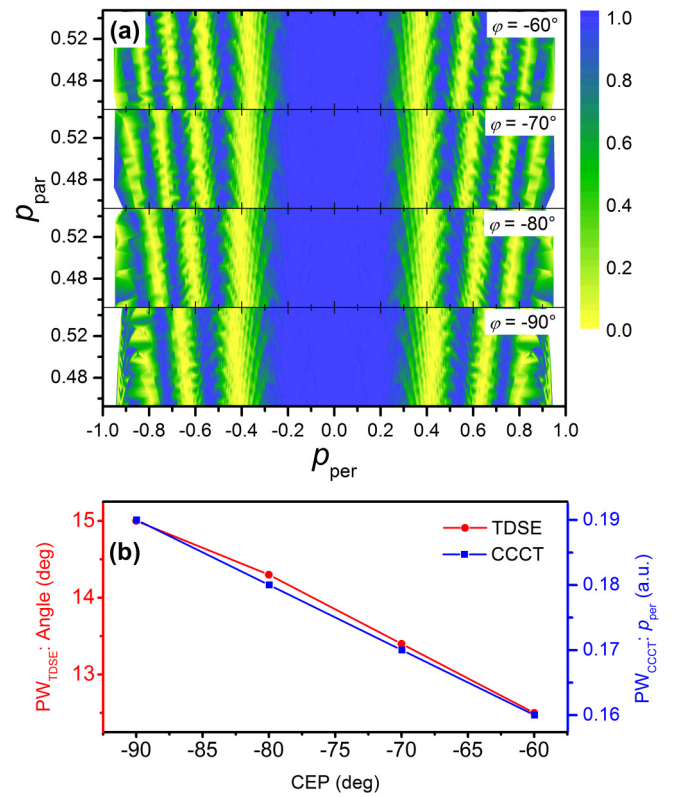
of the carrier envelope almost does not change with the slight variation of the CEP for the ultrashort pulse, but the moment when the electric field or the vector potential equals a specific value changes obviously. Thus, we conjecture that the character of PMD is related to the time information of the trajectory. In Fig. 6(b), we extract the ionization moments of the DTs and STs as functions of the final perpendicular momentum. Here, only the trajectories with a constant final parallel momentum ($p_{\text{par}} = 0.5$ a.u.) are selected for brevity. Obviously, the electrons with the same final perpendicular momentum are ionized later (which means the ionization moment has a large value) progressively when the CEP is changed from $\varphi = -60°$ to $\varphi = -90°$ for both types of electron trajectories, and the delay interval is almost equivalent for any final perpendicular momenta. This is due to the ionization moment appearing successively later for the pulses with CEP of $\varphi = -60°$, $-70°$, $-80°$, and $-90°$. The intersections of the horizontal short black line and the laser vector potentials in Fig. 6(a) show the moments when $A(t) = -0.5$ a.u. [here, $p_{\text{par}} = -A(t_i)$]. In addition, the ionization moments of the DTs are almost invariable, but these of the STs delay obviously with the final perpendicular momentum.
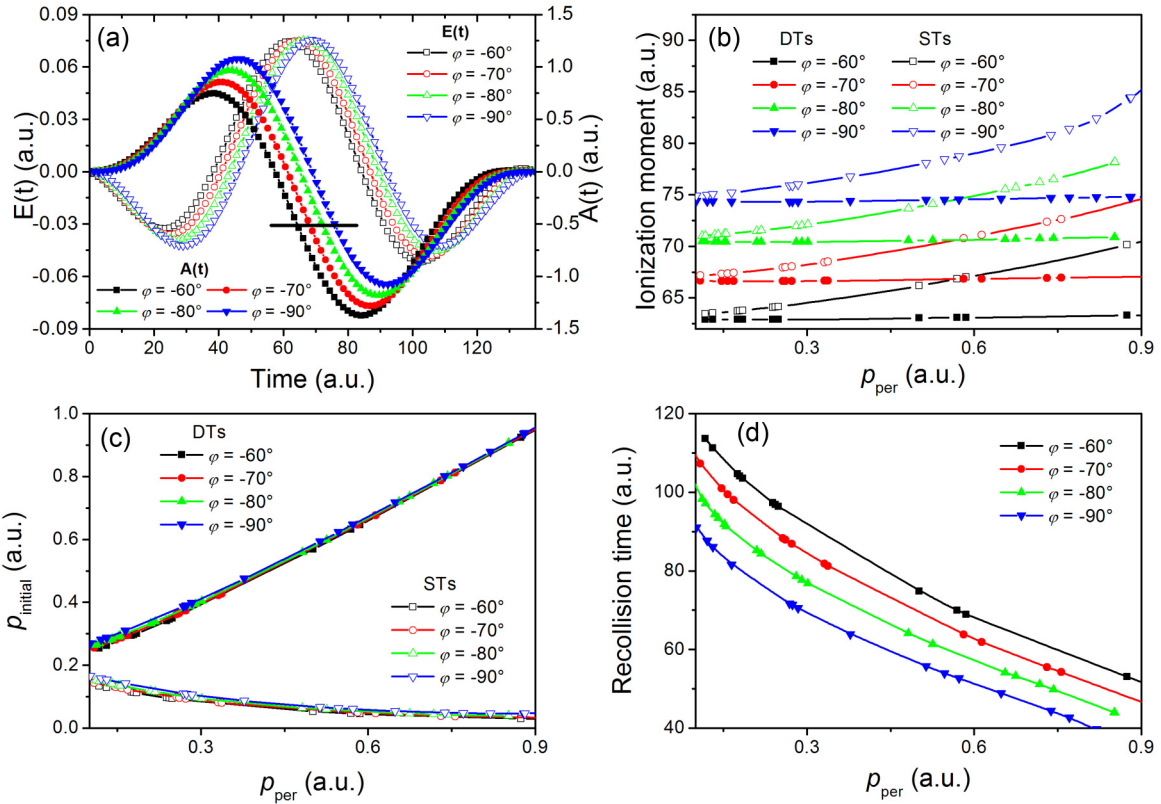
FIG. 6. (a) The electric fields $E(t)$ and their corresponding vector potentials $A(t)$ of single-cycle linearly polarized laser pulses with CEPs of $\varphi = -60°$, $-70°$, $-80°$, and $-90°$. The horizontal short black line implies $A(t) = -0.5$ a.u. (b) The ionization moments of DTs and STs as functions of the final perpendicular momentum (p_{per}) when the final parallel momentum (p_{par}) is equal to 0.5 a.u. (c) The absolute values of the initial perpendicular momenta (p_{ini}) as functions of p_{per} for laser pulses with four different CEPs. Here, $p_{ini} > 0$ for DTs and $p_{ini} < 0$ for STs. (d) The recollision time (RT) of the STs, which means the time interval between the recollision moment and the ionization moment of STs, decreases with p_{per} for all of the four laser pulses. In addition, the RT shortens with the change of CEP from $-60°$ to $-90°$ ($RT_{(-60°)} > RT_{(-70°)} > RT_{(-80°)} > RT_{(-90°)}$) for any one p_{per}. The results are extracted under the condition of $p_{par} = 0.5$ a.u.

First, we discuss the selected DTs with the same final parallel momentum. In the classical simulation, the initial parallel velocity is neglected, so the DTs which are affected by the Coulomb potential weakly are satisfied with the formula $p_{par} = -A(t_i)$, which implies that the ionization moment is independent of the final perpendicular momentum. Then we get the relationship between the final perpendicular momentum and the initial momentum (p_{ini}) which is also perpendicular to the laser polarization direction for the DTs in Fig. 6(c). One can see the weak effect of the Coulomb potential in the perpendicular direction, i.e., $p_{ini} > p_{per}$, and the p_{ini} monotonically increases with p_{per}. Nevertheless, the initial momentum is uniform for the DTs with the same final perpendicular momentum even though the CEP of the laser pulse is different. The trajectory phase defined by Eq. (13) indicates that it is regulated by the ionization moment and the time-dependent velocity. From the above discussion, the ionization time of a DT is related to the laser form and the initial momentum, but is independent of the pulse CEP. We conclude that the ionization moments of DTs affect the interferential structure very weakly.

Unlike DTs, the ionization moments of STs are delayed obviously with the final perpendicular momentum, which indicates that the relation $p_{par} = -A(t_i)$ is ineffective because of the strong effect of the Coulomb potential. We can also see the strong effect from the relationship between the final perpendicular momentum and initial momentum as shown in Fig. 6(c), where $p_{ini} < 0$ for STs and the absolute values are revealed. It is obvious that the final perpendicular momentum can acquire a very high value compared to the low initial momentum due to the collision event, i.e., the lower the initial momentum, the higher the final perpendicular momentum. It is true that the Coulomb potential affects a ST mainly after ionization and before recollision with its parent ion. Figure 6(d) shows the recollision time (RT) which is the time interval between the recollision and ionization moments. One can see that the recollision time decreases with the increase of p_{per} for the four laser pulses. What is more, the recollision time shortens obviously when the CEP is changed from $-60°$ to $-90°$ ($RT_{(-60°)} > RT_{(-70°)} > RT_{(-80°)} > RT_{(-90°)}$) for a specific final momentum. Therefore, the interferential structure or the stripe density in the forward scattering PMD is dominated by the recollision time of the electron, i.e., the longer the recollision time, the greater the stripe density. Actually, this is consistent with the finding of Ref. [43], where the authors showed that the strip density depends on the maximum distance of the electron from the ion before recollision. A long recollision time corresponds to a big distance.
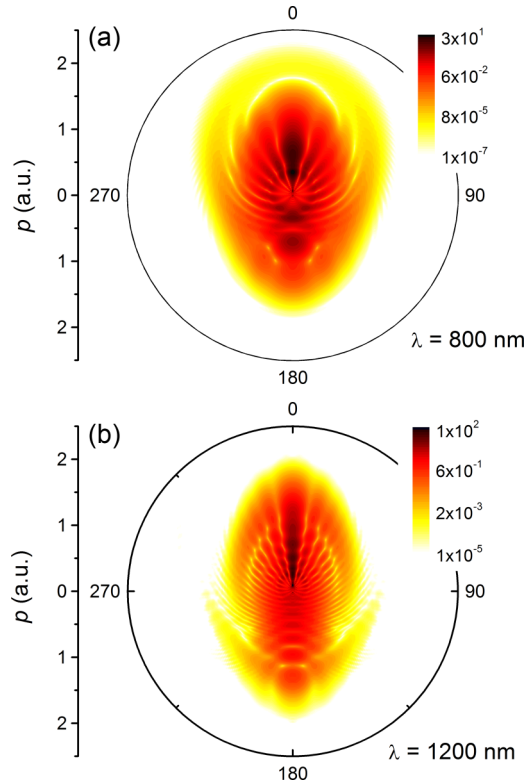
FIG. 7. The PMDs of hydrogen atoms exposed in single-cycle linearly polarized laser pulses with wavelengths of $\lambda = 800$ nm (a) and $\lambda = 1200$ nm (b). The peak intensity and CEP are $I_0 = 2.0 \times 10^{14}$ W/cm^2 and $\varphi = -90°$, respectively.
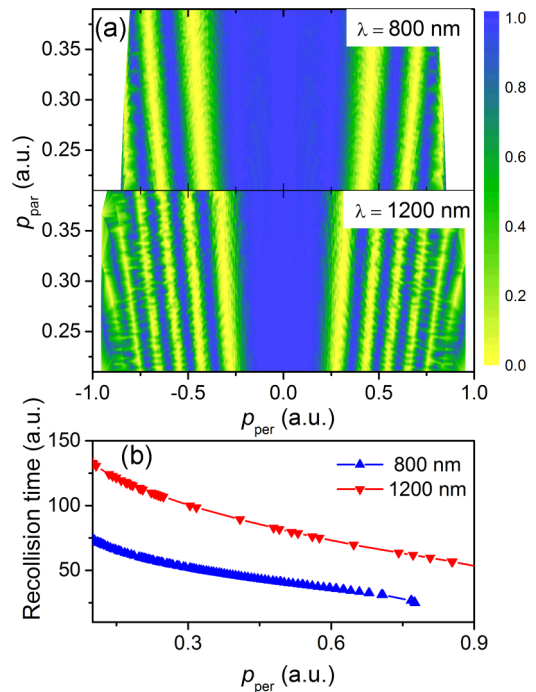

FIG. 8. (a) The interferential structures between the STs and DTs obtained by CCCT for the laser pulses with wavelengths of $\lambda = 800$ nm and $\lambda = 1200$ nm. The other laser parameters are the same as those used in Fig. 7. Here, the range of $0.2 < p_{par} < 0.4$ a.u. is chosen for clear comparison between the two cases. (b) The RT of STs also decrease with the p_{per} increasing for the two laser pulses. The results are extracted under the condition of $p_{par} = 0.3$ a.u.

Finally, we analyze the stripe density of the forward scattering PMD of hydrogen atoms exposed in single-cycle linearly polarized laser pulses with different wavelengths. Figure 7 shows the spider-like patterns with laser wavelengths of $\lambda = 800$ nm and $\lambda = 1200$ nm. The same peak intensity and CEP are 2.0×10^{14} W/cm^2 and $\varphi = -90°$, respectively. It is obvious that the spider legs are much less evident for the pulse with short wavelength than that with long wavelength, which agrees well with the results in Ref. [30]. Meanwhile, we obtain the interferential structure using the CCCT method in the same laser fields, as shown by the comparable patterns in Fig. 8(a). One can see the same tendency as in Fig. 7 that the streaks are denser for the pulse with long wavelength than that with short wavelength. Then, we calculate the recollision times of STs for both cases, where the recollision time is a function of the final perpendicular momentum for a specific final parallel momentum $p_{par} = 0.3$ a.u. We also find that the scattered electrons need a longer time interval to recollide with the parent ion for the laser wavelength of $\lambda = 1200$ nm than that for $\lambda = 800$ nm. Thus, the nature is consistent with the above discussion that the stripe density of the PMD is associated with the recollision time of the scattering electron. Furthermore, the experimental phenomenon in Ref. [18] can be explained easily by this viewpoint; there they reported that the denser spider legs appear because of multiple collisions with the parent ion, and the number of stripes increases with increasing collision time increasing.

IV. CONCLUSION

In summary, we have investigated the recollision of ultrafast electrons from PMDs when a hydrogen atom is ionized by a single-cycle linearly polarized NIR (1000 nm) laser field, based on the numerical solution of the TDSE and classical simulation. The interference pattern in the PMD is closely related to the form of the ultrashort laser pulse which is dominated by the CEP. A fish-bone-like pattern appears in the PMD for the sine electric field where the CEP equals 0°. But when we change the CEP from 0° to $-90°$, an absolutely different spider-like pattern appears. Our results agree with the experimental and theoretical results [17,18]. Then we distinguish the most simple single recollision electrons to investigate the photoelectron scattering dynamics by analyzing the spider-like structures of PMDs. The stripe densities of this pattern are different when the laser CEP is changed slightly. We find that the stripe density is mainly dominated by the recollision time of STs, i.e., the longer the recollision time, the greater the stripe density. In addition, we also provide the PMDs with different wavelengths (800 and 1200 nm). The results reveal that the stripe density is sparser and a shorter recollision time of STs is experienced for the pulse with short wavelength than that with long wavelength. In brief, the PMD interference patterns confirm the direct relation of recollision time and laser frequency in the ionization-scattering dynamics at high intensities, thus allowing also for extraction of the CEP of the ionizing pulse.

[1] F. Krausz and M. Ivanov, Rev. Mod. Phys. **81**, 163 (2009).

[2] M. Y. Ivanov, M. Spanner, and O. Smirnova, J. Mod. Opt. **52**, 165 (2005).

[3] P. B. Corkum, Phys. Rev. Lett. **71**, 1994 (1993).

[4] R. P. Sun, X. Y. Lai, S. G. Yu, Y. L. Wang, S. P. Xu, W. Quan, and X. J. Liu, Phys. Rev. Lett. **122**, 193202 (2019).

[5] K. J. Schafer, B. Yang, L. F. DiMauro, and K. C. Kulander, Phys. Rev. Lett. **70**, 1599 (1993).

[6] Q. Z. Xia, J. F. Tao, J. Cai, L. B. Fu, and J. Liu, Phys. Rev. Lett. **121**, 143201 (2018).

[7] M. Lewenstein, P. Balcou, M. Y. Ivanov, A. L'Huillier, and P. B. Corkum, Phys. Rev. A **49**, 2117 (1994).

[8] W. Becker, F. Grasbon, R. Kopold, D. B. Milošević, G. G. Paulus, and H. Walther, in *Above-Threshold Ionization: From Classical Features to Quantum Effects*, edited by B. Bederson and H. Walther (Academic Press, New York, 2002), Vol. 48, pp. 35–98.

[9] W. Becker, X. J. Liu, P. J. Ho, and J. H. Eberly, Rev. Mod. Phys. **84**, 1011 (2012).

[10] J. J. Barton, Phys. Rev. Lett. **61**, 1356 (1988).

[11] D. M. Villeneuve, P. Hockett, M. J. J. Vrakking, and H. Niikura, Science **356**, 1150 (2017).

[12] J. Mauritsson, P. Johnsson, E. Mansten, M. Swoboda, T. Ruchon, A. L'Huillier, and K. J. Schafer, Phys. Rev. Lett. **100**, 073003 (2008).

[13] T. Remetter, P. Johnsson, J. Mauritsson, K. Varjú, Y. Ni, F. Lépine, E. Gustafsson, M. Kling, J. Khan, R. López-Martens, K. J. Schafer, M. J. J. Vrakking, and A. L'Huillier, Nat. Phys. **2**, 323 (2006).

[14] D. Gabor, Nature (London) **161**, 777 (1948).

[15] C. Figueira de Morisson Faria and A. S. Maxwell, Rep. Prog. Phys. **83**, 034401 (2020).

[16] Y. Huismans, A. Rouzée, A. Gijsbertsen, J. H. Jungmann, A. S. Smolkowska, P. S. W. M. Logman, F. Lépine, C. Cauchy, S. Zamith, T. Marchenko, J. M. Bakker, G. Berden, B. Redlich, A. F. G. van der Meer, H. G. Muller, W. Vermin, K. J. Schafer, M. Spanner, M. Y. Ivanov, O. Smirnova, D. Bauer, S. V. Popruzhenko, and M. J. J. Vrakking, Science **331**, 61 (2011).

[17] Y. Huismans, A. Gijsbertsen, A. S. Smolkowska, J. H. Jungmann, A. Rouzée, P. S. W. M. Logman, F. Lépine, C. Cauchy, S. Zamith, T. Marchenko, J. M. Bakker, G. Berden, B. Redlich, A. F. G. van der Meer, M. Y. Ivanov, T. M. Yan, D. Bauer, O. Smirnova, and M. J. J. Vrakking, Phys. Rev. Lett. **109**, 013002 (2012).

[18] D. D. Hickstein, P. Ranitovic, S. Witte, X.-M. Tong, Y. Huismans, P. Arpin, X. Zhou, K. E. Keister, C. W. Hogle, B. Zhang, C. Ding, P. Johnsson, N. Toshima, M. J. J. Vrakking, M. M. Murnane, and H. C. Kapteyn, Phys. Rev. Lett. **109**, 073004 (2012).

[19] X.-B. Bian, Y. Huismans, O. Smirnova, K.-J. Yuan, M. J. J. Vrakking, and A. D. Bandrauk, Phys. Rev. A **84**, 043420 (2011).

[20] X.-B. Bian and A. D. Bandrauk, Phys. Rev. Lett. **108**, 263003 (2012).

[21] M. Haertelt, X.-B. Bian, M. Spanner, A. Staudte, and P. B. Corkum, Phys. Rev. Lett. **116**, 133001 (2016).

[22] N. I. Shvetsov-Shilovski and M. Lein, Phys. Rev. A **97**, 013411 (2018).

[23] S. G. Yu, X. Y. Lai, Y. L. Wang, S. P. Xu, L. Q. Hua, W. Quan, and X. J. Liu, Phys. Rev. A **101**, 023414 (2020).

[24] G. Porat, G. Alon, S. Rozen, O. Pedatzur, M. Krüger, D. Azoury, A. Natan, G. Orenstein, B. D. Bruner, M. J. J. Vrakking, and N. Dudovich, Nat. Commun. **9**, 2805 (2018).

[25] S. G. Walt, N. Bhargava Ram, M. Atala, N. I. Shvetsov-Shilovski, A. von Conta, D. Baykusheva, M. Lein, and H. J. Wörner, Nat. Commun. **8**, 15651 (2017).

[26] S. Borbély, A. Tóth, D. G. Arbó, K. Tőkési, and L. Nagy, Phys. Rev. A **99**, 013413 (2019).

[27] S. D. López and D. G. Arbó, Phys. Rev. A **100**, 023419 (2019).

[28] D. G. Arbó, E. Persson, and J. Burgdörfer, Phys. Rev. A **74**, 063407 (2006).

[29] R. Gopal, K. Simeonidis, R. Moshammer, T. Ergler, M. Dürr, M. Kurka, K. U. Kühnel, S. Tschuch, C. D. Schröter, D. Bauer, J. Ullrich, A. Rudenko, O. Herrwerth, T. Uphues, M. Schultze, E. Goulielmakis, M. Uiberacker, M. Lezius, and M. F. Kling, Phys. Rev. Lett. **103**, 053001 (2009).

[30] M. Murakami and G.-P. Zhang, Phys. Rev. A **101**, 053439 (2020).

[31] S. Chelkowski, C. Foisy, and A. D. Bandrauk, Phys. Rev. A **57**, 1176 (1998).

[32] M. Yuan, R. Lü, L. Feng, and T. Chu, J. Chem. Phys. **140**, 074108 (2014).

[33] R.-F. Lu, P.-Y. Zhang, and K.-L. Han, Phys. Rev. E **77**, 066701 (2008).

[34] M. H. Beck, A. Jackle, G. A. Worth, and H. D. Meyer, Phys. Rep. **324**, 1 (2000).

[35] M. Murakami and S.-I Chu, Phys. Rev. A **93**, 023425 (2016).

[36] X. M. Tong, K. Hino, and N. Toshima, Phys. Rev. A **74**, 031405(R) (2006).

[37] M.-H. Yuan and X.-B. Bian, Phys. Rev. A **101**, 013412 (2020).

[38] M. V. Ammosov, N. B. Delone, and V. P. Krainov, Zh. Eksp. Teor. Fiz. **91**, 2008 (1986) [Sov. Phys. JETP **64**, 1191 (1986)].

[39] F. Lindner, M. G. Schätzel, H. Walther, A. Baltuška, E. Goulielmakis, F. Krausz, D. B. Milošević, D. Bauer, W. Becker, and G. G. Paulus, Phys. Rev. Lett. **95**, 040401 (2005).

[40] N. I. Shvetsov-Shilovski, M. Lein, L. B. Madsen, E. Räsänen, C. Lemell, J. Burgdörfer, D. G. Arbó, and K. Tökési, Phys. Rev. A **94**, 013415 (2016).

[41] I. Samengo and R. O. Barrachina, J. Phys. B **29**, 4179 (1996).

[42] R. C. Fuller, Phys. Rev. C **12**, 1561 (1975).

[43] S. Borbély, A. Tóth, K. Tökési, and L. Nagy, Phys. Rev. A **87**, 013405 (2013).